micromachines

MDPI

Article

Application of Micro-Arc Discharges during Anodization of Tantalum for Synthesis of Photocatalytic Active Ta_2O_5 Coatings

Stevan Stojadinović [1,2,*], Nenad Radić [3] and Rastko Vasilić [1]

[1] Faculty of Physics, University of Belgrade, Studentski trg 12-16, 11000 Belgrade, Serbia
[2] Faculty of Forestry, University of Belgrade, Kneza Višeslava 1, 11000 Belgrade, Serbia
[3] IChTM-Department of Catalysis and Chemical Engineering, University of Belgrade, Njegoševa 12, 11000 Belgrade, Serbia
* Correspondence: sstevan@ff.bg.ac.rs; Tel.: +381-11-7158161

Abstract: Ta_2O_5 coatings were created using micro-arc discharges (MDs) during anodization on a tantalum substrate in a sodium phosphate electrolyte (10 g/L $Na_3PO_4 \cdot 10H_2O$). During the process, the size of MDs increases while the number of MDs decreases. The elements and their ionization states present in MDs were identified using optical emission spectroscopy. The hydrogen Balmer line H_β shape analysis revealed the presence of two types of MDs, with estimated electron number densities of around 1.1×10^{21} m^{-3} and 7.3×10^{21} m^{-3}. The effect of MDs duration on surface morphology, phase and chemical composition, optical absorption, and photoluminescent, properties of Ta_2O_5 coatings, as well as their applications in photocatalytic degradation of methyl orange, were investigated. The created coatings were crystalline and were primarily composed of Ta_2O_5 orthorhombic phase. Since Ta_2O_5 coatings feature strong absorption in the ultraviolet light region below 320 nm, their photocatalytic activity is very high and increases with the time of the MDs process. This was associated with an increase of oxygen vacancy defects in coatings formed during the MDs, which was confirmed by photoluminescent measurements. The photocatalytic activity after 8 h of irradiation was around 69%, 74%, 80%, and 88% for Ta_2O_5 coatings created after 3 min, 5 min, 10 min, and 15 min, respectively.

Keywords: micro-arc discharges; plasma electrolytic oxidation; micro-arc oxidation; tantalum; Ta_2O_5; photocatalysis; optical emission spectroscopy

Citation: Stojadinović, S.; Radić, N.; Vasilić, R. Application of Micro-Arc Discharges during Anodization of Tantalum for Synthesis of Photocatalytic Active Ta_2O_5 Coatings. *Micromachines* **2023**, *14*, 701. https://doi.org/10.3390/mi14030701

Academic Editor: Marija Radmilović-Radjenović

Received: 15 February 2023
Revised: 17 March 2023
Accepted: 20 March 2023
Published: 22 March 2023

1. Introduction

Tantalum pentoxide (Ta_2O_5) is a transition metal oxide with exceptional physical and chemical properties, including high dielectric constant and refractive index, low optical absorption coefficient, excellent photoelectric performance, and good chemical stability [1–3]. These properties are used in a variety of Ta_2O_5 applications, including memory devices, coatings on photographic lenses, electrochromic devices, biocompatible materials, photocatalysts, etc. [4–8].

The goal of this study was to examine the possibility of synthesizing Ta_2O_5 coatings on tantalum substrates using micro-arc discharges (MDs) during anodization for applications in organic pollutant degradation. The process of the formation of oxide coatings under MDs is known as micro-arc oxidation (MAO) or plasma electrolytic oxidation (PEO) [9–12]. The elevated local temperature (10^3 K to 10^4 K) and pressure (up to 10^2 MPa) cause numerous processes, including light and heat emission, thermal, electrochemical, and plasma-chemical reactions to take place at the MD sites [13]. The structure, content, and morphology of the produced oxide coatings are changed as a result of these processes. The coatings produced are primarily composed of substrate oxides, but more complex compounds involving the species present in the electrolyte can also be formed [10].

The formation of oxide coatings is accomplished through several steps [14]. As a result of dielectric stability loss in a low conductivity region, a number of separated MD channels

are formed in the oxide layer during the first step. This region is heated to temperatures of 10^4 K by generated electron avalanches [15]. The anionic components of the electrolyte are drawn into the channels by the strong electric field. At the same time, the metal is melted out of the substrate, enters the MD channels, and oxidizes. Plasma-chemical reactions occur in the MD channels as a result of these processes. At the same time, the presence of an electric field causes the separation of oppositely charged ions in the MD channels. Electrostatic forces eject the cations from the MD channels into the electrolyte. The oxidized metal is then ejected from the MD channels into the coating surface in contact with the electrolyte, increasing the coating thickness around the MD channels. Finally, the MD channels cool, and the reaction products are deposited on their walls. This process is repeated at a number of discrete locations across the coating surface, resulting in an increase in coating thickness. The coating material formed at the MD sites consists of crystalline and amorphous phases, with constituent species derived from both the metal and the electrolyte.

Semiconductor photocatalysis is currently regarded as one of the most promising solar energy conversion technologies for organic pollution degradation. Transition metal oxides such as TiO_2 and ZnO are the primary photocatalysts that exhibit high efficiency for photocatalytic processes [16–18]. Additionally, some other transition metal oxides are used in photocatalytic processes, such as WO_3 [19], V_2O_5 [20], ZrO_2 [21], Nb_2O_5 [22], and Ta_2O_5 [23]. Ta_2O_5 has received a lot of attention among these transition metal oxides as a highly desirable replacement for TiO_2 and ZnO. Because of the properly positioned band gap of Ta_2O_5 [24], it is possible to perform the majority of photocatalytic reactions without the use of additional components and compounds. Furthermore, its conduction band is higher than TiO_2 and ZnO, providing more favorable conditions for the smooth continuation or initiation of reduction reactions [23]. The main disadvantage of the Ta_2O_5 photocatalyst is its large gap (around 4 eV), which necessitates the use of strong ultraviolet light (below 310 nm) for photocatalytic reactions [23].

The majority of studies have focused on the Ta_2O_5 photocatalysts in powder form, which is difficult to separate after reaction and unsuitable for recycling [25–28]. This problem can be solved by focusing on Ta_2O_5-based photocatalysts supported on a stable substrate. Our research has shown that efficient photocatalysts on various metal substrates can be obtained using MDs during their anodization in suitable electrolytes [29–31]. So far, several papers have been published that investigate oxide coatings formed on tantalum substrates under MDs, primarily for biomedical applications [32–37]. In this paper, we demonstrate for the first time that the coatings formed on tantalum substrates under MDs can be used as photocatalysts for organic pollutant degradation.

2. Materials and Methods

Commercial tantalum foils (99.9% purity) with a thickness of 0.25 mm were used as a starting material and were cut into samples with dimensions of 10 mm × 25 mm. Before processing, the samples were ultrasonically cleaned for 5 min in acetone, dried with a warm air stream, and covered with insulating resin to provide a working area of 10 mm × 15 mm. More details about the experimental setup can be found in Ref. [38]. In short, the electrolytic cell was a 250 mL double-walled glass cell with water cooling. The temperature of the electrolyte was kept within (20 ± 1) °C. Tantalum samples were used as anodes and positioned in the center of the electrolytic cell, surrounded by a tubular stainless-steel cathode. The process was carried out in direct current mode with a current density of 150 mA/cm^2 for varying times up to 15 min using a Consort EV261 DC power unit. The electrolyte was a water solution containing 10 g/L $Na_3PO_4 \cdot 10H_2O$.

The morphology and elemental analyses of the coatings were performed using a scanning electron microscope (SEM, JEOL 840A, Tokyo, Japan) with energy-dispersive X-ray spectroscopy (EDS, Oxford INCA, Abingdon, UK). The phase composition of the coatings was identified by X-ray diffraction (XRD, Rigaku Ultima IV, Tokyo, Japan) using a monochromatic Cu Kα radiation. The coating surface was additionally analyzed by a X-ray

photoelectron spectroscopy (XPS, SPECS System, Germany) using a monochromatic Al K_α radiation. Binding energies were corrected relative to the C 1s signal at 285.0 eV. The optical properties of coatings were analyzed by UV-Vis diffuse reflectance spectra (DRS, Shimadzu UV-3600, Tokyo, Japan) and photoluminescence (PL, Horiba Jobin Yvon Fluorolog FL3-22, Edison, NJ, USA) using a 450 W xenon lamp as the excitation light source.

To test the photocatalytic activity (PA) of formed coatings, the photodegradation of methyl orange (MO), as the model compound for organic pollution, was examined under artificial solar radiation at 20 °C. To achieve absorption–desorption equilibrium, a solution containing 8 mg/L of MO was left in the dark for one hour in a 6.8 cm diameter open cylindrical thermostated pyrex glass reactor. MO adsorption was minimal as evidenced by the nearly constant MO concentration. The samples were then illuminated by a 300 W lamp (OSRAM ULTRA-VITALUX UV-A, Germany) that was positioned 25 cm above the solution's top surface. The samples were positioned 5 mm above the reactor bottom on the steel wire holder. Monitoring MO decomposition at predetermined intervals after exposure to irradiation allowed for the estimation of PA. The maximum MO absorption peak at 464 nm was used to measure the MO concentration using a UV-Vis spectrophotometer (Thermo Electron Nicolet Evolution 500, UK).

3. Results and Discussion

Figure 1 depicts the voltage–time response during galvanostatic anodization of tantalum. The voltage increases approximately linearly with time from the start of anodization to about 300 V in a very short time resulting in a constant rate of increase of the oxide film thickness [39]. This is followed by an apparent deviation from linearity in the voltage-time curve, beginning with the so-called sparking (breakdown) voltage. Following the breakdown, the voltage continues to rise, but the voltage–time slope drops, and a large number of small size MDs appear, evenly distributed across the entire sample surface. Further anodization results in a relatively stable value of the anodization voltage.

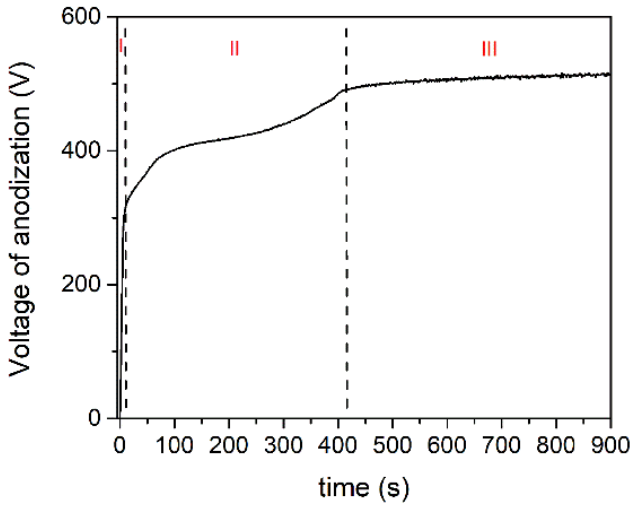

Figure 1. Voltage-time curve during anodization of tantalum at 150 mA/cm^2 in $Na_3PO_4 \cdot 10H_2O$.

The process of tantalum anodization can be separated into three stages based on the voltage–time response. Total anodizing current density is the sum of ionic and electron current densities [40]. During the anodic growth in stage I, the electric field strength for a certain current density remains constant, and the ionic current is two to three orders of magnitude higher than the electronic component. To keep the electric field strength constant, the voltage of anodization must increase linearly as the film thickens. In addition, during anodization, electrons are injected into the anodic oxide's conduction band and accelerated by the electric field, resulting in avalanches via an impact ionization mechanism [40]. The breakdown occurs when the avalanche electronic current reaches a critical value [41]. Due

to the independence of electron current density with anodic oxide film thickness, a relatively low voltage is required in stage II to maintain the same total current density (compared to stage I). The fraction of electron current density in total current density becomes dominant in stage III. The total current density is almost independent of the oxide film thickness at this stage, and the voltage–time slope is close to zero.

Figure 2 depicts the appearance of MDs at various stages of the anodization process. MDs were visible after about 10 s from the onset of anodization. As the duration of the process lengthens, the size of MDs increases while the number of MDs decreases. Given that MDs are generated by dielectric breakdown through weak sites in the oxide coating, the number of weak sites decreases as anodization time, i.e., coating thickness, increases. The increased size of MDs with increasing PEO time was attributed to a reduced number of MDs sites through which higher anodic current can pass [9]. The MDs gradually vanished after 15 min, rendering the process ineffective.

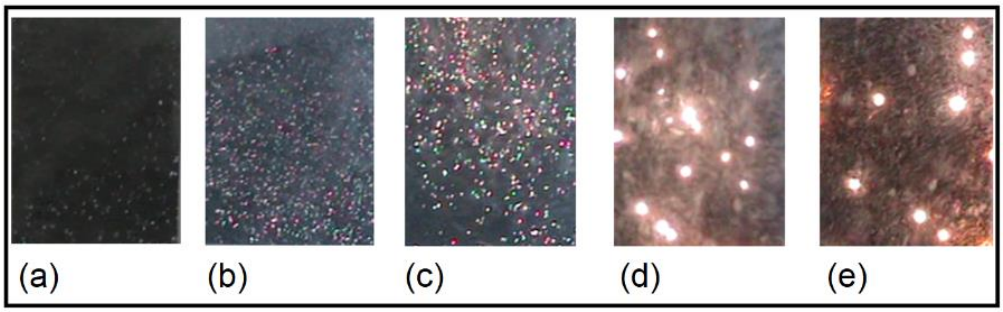

Figure 2. MDs appearance at various stages of tantalum anodization: (**a**) 10 s; (**b**) 150 s; (**c**) 300 s; (**d**) 600 s; (**e**) 900 s.

Figure 3a depicts a typical optical emission spectrum of MDs in the spectral range 400 nm to 850 nm. The sodium doublet spectral lines Na I at 588.99 nm and 589.59 nm were the most intense. Additionally, detected was a relatively strong hydrogen Balmer line H_α (656.28 nm). The continuum emission was caused by electron collision-radiative recombination [39] and bremsstrahlung radiation [42]. There were some weak lines that corresponded to neutral oxygen atoms (O I) in the range from 700 nm to 850 nm (Figure 3c) and singly ionized oxygen atoms (O II), as well as the Balmer line H_β (486.13 nm), in the range from 400 nm to 500 nm (Figure 3b). However, no lines were observed from the species present in the substrate, indicating that tantalum's high melting point prevented its evaporation during MDs.

Strong sodium doublet spectral lines [43] and Balmer line H_α [44] are not suitable for the spectral line shape analysis. The broadened profile of the Balmer H_β line was used for MDs electron number density measurements. During the analysis of the H_β line profile (Figure 3d), it was discovered that the H_β line shape could only be properly fitted using two Lorentzian profiles. The upper part of the H_β profile has a full width at half maximum (FWHM) of 0.23 nm, while the broad lower profile has an FWHM of 0.81 nm. This is in agreement with empirical formula (2a) in [45], which yields electron number densities of ~1.1×10^{21} m^{-3} and ~7.3×10^{21} m^{-3}. Two different electron number densities most likely indicate the presence of two MDs processes: MDs in relatively small holes near the surface of the oxide layer and MDs in micro-pores near the surface of the oxide layer [46].

Top view and cross-section SEM micrographs of the oxide of coatings formed at various stages of the MDs are shown in Figure 4. The presence of pores of various diameters, shapes, and molten regions distributed throughout the surface characterize the coatings formed during MDs. The pores are associated with the release of gas bubbles from MD channels, whereas molten regions are formed as a result of heating, melting, and quenching of the molten oxide in contact with the surrounding electrolyte, resulting in an increase of surface roughness during MDs [9]. Dense layers, with an average thickness of about 5.9 μm,

8.3 µm, 9.2 µm, and 11.2 µm, were formed after 3 min, 5 min, 10 min, and 15 min of MDs, respectively.

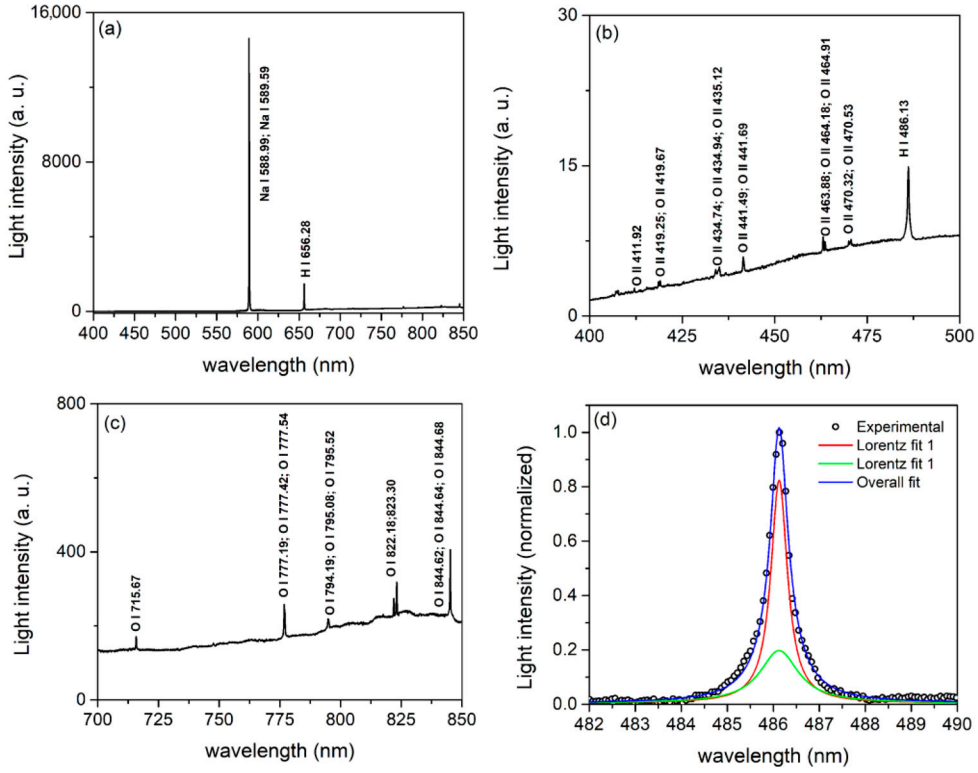

Figure 3. Optical emission spectra of MDs during anodization of tantalum in the range: (**a**) 400–850 nm; (**b**) 400–500 nm; (**c**) 700–850 nm; (**d**) The H_β line profile fitted with two Lorentzian profiles.

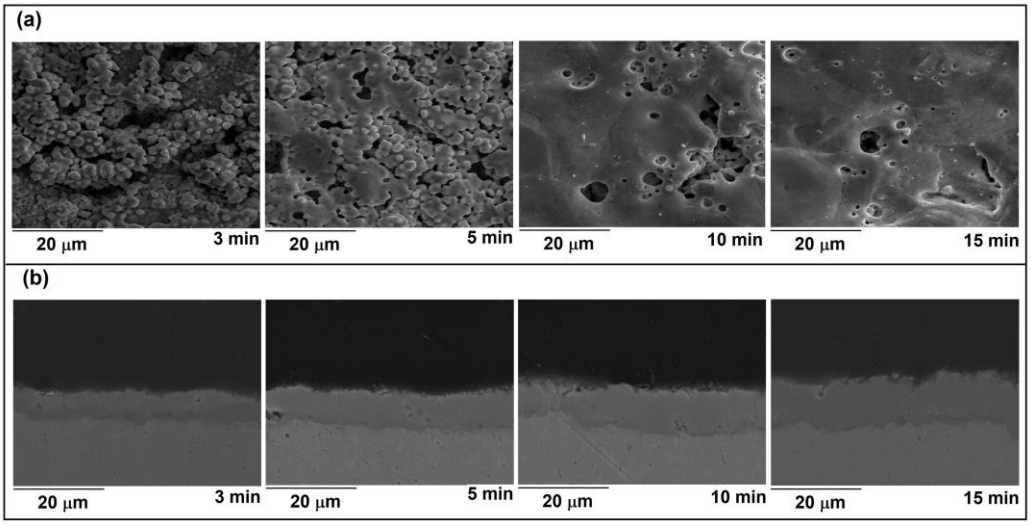

Figure 4. (**a**) Top view; (**b**) cross-section; micrographs of coatings formed at various stages of the MDs.

Table 1 displays the results of the integral EDS analyses of surface coatings (the relative errors are less than 5%) shown in Figure 4a. Ta, O, and P are the primary components of the coatings. Ta substrate and electrolyte interactions during MDs lead to the observed chemical composition. P was incorporated into the coatings as a result of PO_4^{3-} ion movement to the Ta anode and reaction with the molten oxidized metal.

Table 1. EDS elemental analysis of coatings in Figure 4a.

MDs Time (Min)	Atomic (%)		
	O	P	Ta
3	74.62	5.06	20.32
5	75.41	3.99	20.60
10	74.31	3.81	21.87
15	74.75	3.60	21.64

It is widely accepted that Ta_2O_5 has two main polymorphs, which are usually referred to as high-temperature and low-temperature phases [23]. The transition usually occurs at 1360 °C and this process is reversible, which means that the high-temperature phase cannot be stabilized. As a result, the low-temperature phase is more appealing because it can exist at ambient temperatures. It usually exists in the form of an orthorhombic or hexagonal crystal structure, with the former one being more stable. The XRD patterns of formed coatings are presented in Figure 5. Orthorhombic Ta_2O_5 (JCPDS, No. 25-0922) was identified as the main crystalline phase in all of the coatings. This suggests that the rapid solidification of molten Ta_2O_5 flowing out of the MD channels in the presence of a low temperature electrolyte promotes the formation of orthorhombic Ta_2O_5. The XRD pattern of coating formed for 15 min also contains a few diffraction lines with low intensities, probably connected with tantalum phosphate phases.

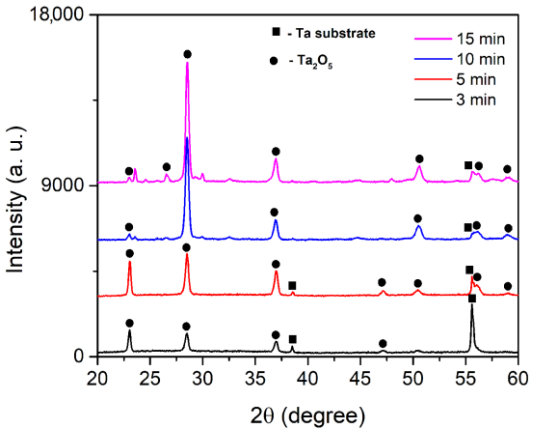

Figure 5. XRD patterns of coatings formed at various stages of the MDs.

We used XPS measurements of coating formed for 15 min to further investigate the chemical nature, composition, and oxidation state of Ta, O, and P (Figure 6). Figure 6a depicts typical survey XPS spectra, which confirm the presence of peaks originating from Ta 4f, Ta 4d, Ta 4p, O 1s, P 2s, P 2p, and C 1. Figure 6 also includes high-resolution XPS spectra of Ta 4f, P 2p, and O 1s. The high-resolution Ta 4f XPS spectrum can be fitted into two components with peaks at 26.31 eV and 28.19 eV, which correspond to Ta $4f_{7/2}$ and Ta $4f_{5/2}$ spin orbit splitting, respectively. These peaks' binding energy positions indicate the presence of Ta species in the form of Ta^{5+} [25]. The high resolution P 2p XPS spectrum can also be fitted into two components with peaks at 133.64 eV and 134.59 eV, which correspond to the binding energies of $2p_{3/2}$ and $2p_{1/2}$ phosphorus levels in the P^{5+} valence state [47]. The high resolution O 1s XPS spectrum can be deconvoluted into two components at 530.37 eV and 531.35 eV, indicating two distinct oxide environments: oxygen bonded to phosphorous (530.37 eV) and oxygen bonded to tantalum (531.35 eV) [48].

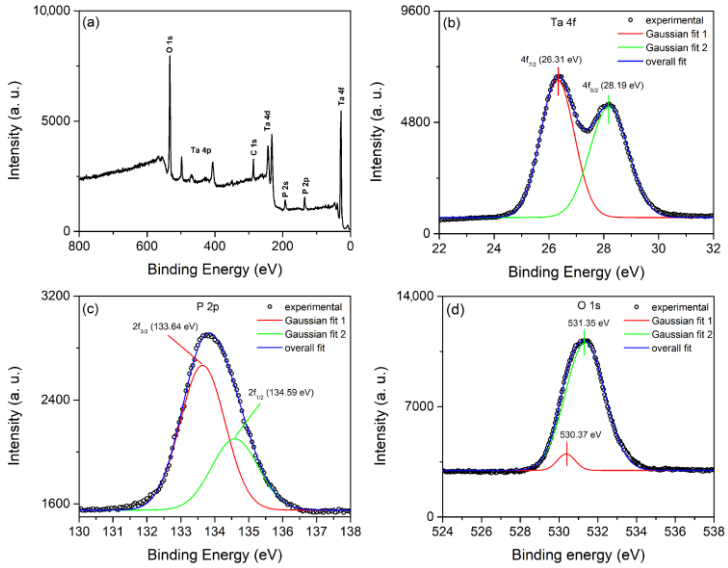

Figure 6. (**a**) Survey XPS spectrum of coating formed for 900 s. High resolution XPS spectra: (**b**) Ta 4f; (**c**) P 2p; (**d**) O 1s.

The photocatalytic performance of Ta_2O_5 coatings was tested in MO degradation. Three samples were tested for each processing time, with the mean values shown in Figure 7a. The PA of samples obtained under the same conditions is highly reproducible (within 3%). *Co* represents the initial concentration of MO, whereas *C* represents the concentration after time *t*. The coating with the highest photocatalytic efficiency was formed for 15 min. Ta_2O_5 coatings have a much higher efficiency in MO degradation than TiO_2 [49], MgO [50], MgAl [38], ZrO_2 [51], and Nb_2O_5 [52] coatings formed under MDs on titanium, AZ31 magnesium alloy, zirconium, and niobium substrate, respectively (Figure 7b).

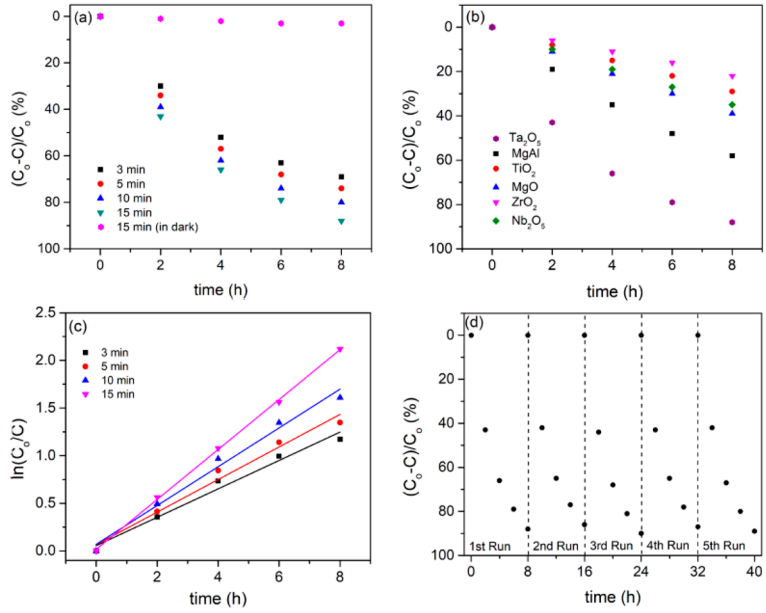

Figure 7. (**a**) PA of Ta_2O_5 coatings formed at various stages of the MDs; (**b**) PA for different coatings formed by MDs process; (**c**) First-order kinetic plots of Ta_2O_5 coatings formed at various stages of the MDs; (**d**) Recycling test of MO photodegradation of coating formed for 15 min.

The photocatalytic degradation rate of Ta_2O_5 coatings was calculated using the first-order kinetic Langmuir Hinshelwood model (Figure 7c):

$$ln\left(\frac{C_o}{C}\right) = k_{app}t \quad (1)$$

The first-order kinetic constant k_{app} and the corresponding linear correlation coefficient (R^2) are shown in Table 2. As the time of the MDs process increased from 3 min to 15 min, the k_{app} increased from 0.146 h^{-1} to 0.262 h^{-1}.

Table 2. First-order kinetic constant k_{app} and corresponding linear correlation coefficient R^2 for Ta_2O_5 coatings formed at various stages of the MDs.

Time of MDs (Min)	3	5	10	15
k_{app} (h^{-1})	0.146	0.171	0.204	0.262
R^2	0.974	0.974	0.982	0.999

The chemical and physical stability of photocatalysts during photocatalytic reactions are critical issues for practical applications. To assess the cycling stability of Ta_2O_5 coatings, photodegradation on MO was cycled five times with the most active photocatalyst as a representative sample (Figure 7d). The sample was rinsed with water, dried, and reused after each photocatalytic run. Photocatalytic deactivation clearly does not occur, demonstrating the dependability and effectiveness of Ta_2O_5 coatings formed under MDs as photocatalysts.

The main contribution of MDs time to the PA of Ta_2O_5 coatings could be either in extending the optical absorption range of Ta_2O_5 coatings or in preventing fast recombination process of photogenerated electron/hole pairs, given that MDs time has slight effect on the phase structure of Ta_2O_5 coatings. Ultraviolet-visible DRS was used to investigate the light absorption properties of formed Ta_2O_5 coatings. As shown in Figure 8a, all of the samples have a distinct absorption band in the ultraviolet range, with the light absorption edge at about 320 nm, which is associated with the transition from the O 2p orbital to the empty Ta 5d orbitals [23], while the best ultraviolet absorption capacity has the thickest coating formed for 15 min of PEO. These findings suggest that Ta_2O_5 coatings can be active in photocatalytic reactions when exposed to ultraviolet light. This limits its ability to absorb only 4–5% of the sunlight. Such poor sunlight absorption capability has little practical application for the Ta_2O_5 photocatalysis.

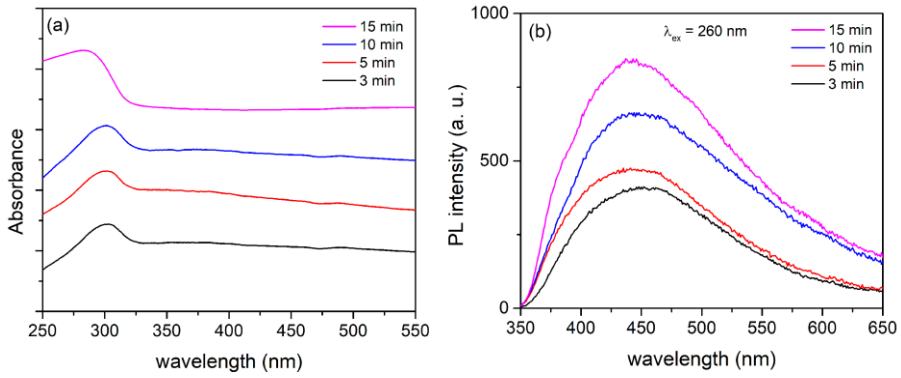

Figure 8. (**a**) DRS spectra; (**b**) PL emission spectra; Ta_2O_5 coatings formed at various stages of the MDs.

The significant PA of Ta_2O_5 is probably related to the high concentration of different types of surface vacancies and other defects in the formed coatings during MDs. Surface vacancies, which control the electron transfer between reactants and photocatalysts, are closely related to active centers of heterogeneous photocatalytic reactions [53,54]. PL

spectroscopy is an effective optical technique for detecting oxygen vacancies and other defects in semiconductor materials [55]. The PL emission spectra of formed Ta_2O_5 coatings excited at 260 nm are shown in Figure 8b. The PL intensity rises with increasing MDs time, suggesting that thicker coatings have higher oxygen vacancies and defect concentrations [56,57]. Throughout the PL process, oxygen vacancies and defects could bind photo-induced electrons to form free or binding excitons, allowing a PL signal to occur easily, and the higher the oxygen vacancy or defect content, the stronger the PL intensity [56,57]. However, during the photocatalysis, oxygen vacancies and defects may serve as capture sites for photo-induced electrons, effectively inhibiting photo-induced electron and hole recombination, which leads to an increase in PA of Ta_2O_5 coatings. Furthermore, oxygen vacancies can stimulate O_2 adsorption, and photo-induced electrons bound by oxygen vacancies interact strongly with adsorbed O_2 [55]. This suggests that oxygen vacancies can help adsorbed O_2 capture photo-induced electrons while also producing $\cdot O_2$ radical groups. The radical groups are active in promoting the oxidation of organic pollutants. Thus, oxygen vacancies and defects may favor photocatalytic reactions, and the stronger the excitonic PL intensity, the greater the oxygen vacancy or defect content, and the higher the photocatalytic activity.

4. Conclusions

Ta_2O_5 coatings were created using MDs during tantalum anodization in a sodium phosphate electrolyte for varying times. MDs were characterized using real-time images and optical emission spectroscopy. SEM/EDS, XRD, XPS, DRS, and PL were used to investigate the morphology, crystal structure, chemical composition, and optical properties of Ta_2O_5 coatings. The photodegradation of MO in simulated sunlight was used to assess the photocatalytic potential of Ta_2O_5 coatings.

The following conclusions can be drawn:

With increasing anodization time, the size of MDs increases while the number of MDs decreases. The species identified by optical emission spectroscopy under MD originate only from the electrolyte and belong to sodium, hydrogen, and oxygen. In the hydrogen Balmer line H_β shape analysis, two types of MDs were revealed that were connected to MDs at the oxide–electrolyte interface, with electron number densities of approximately 1.1×10^{21} m^{-3} and 7.3×10^{21} m^{-3}.

The morphology of created coatings is determined by the MDs time. The chemical elements of the coatings are Ta, O, and P. Ta and P have pentavalent oxidation states, according to XPS measurements. The created coatings are crystalline and primarily comprised of the orthorhombic Ta_2O_5 phase. Ta_2O_5 coatings have a broad absorption band in the ultraviolet light region below 320 nm.

The PA of Ta_2O_5 coatings depends on the time of creation during MDs. The best photocatalytic performance was observed for the coating processed for 15 min. Ta_2O_5 coatings have a much higher efficiency in MO degradation than TiO_2, MgO, MgAl, ZrO_2, and Nb_2O_5 coatings formed under MDs on titanium, AZ31 magnesium alloy, zirconium, and niobium substrate, respectively.

Author Contributions: Conceptualization, S.S.; methodology, S.S.; validation, S.S., investigation, S.S., N.R. and R.V.; writing—original draft preparation, S.S.; writing—review and editing, S.S., N.R. and R.V. All authors have read and agreed to the published version of the manuscript.

Funding: This research was funded by the Ministry of Science, Technological Development and Innovation of the Republic of Serbia (Grants 451-03-47/2023-01/200162 and 451-03-47/2023-01/200026) and by the European Union Horizon 2020 Research and Innovation program under the Marie Sklodowska-Curie grant agreement No. 823942 (FUNCOAT).

Data Availability Statement: The data presented in this study are available on request from the corresponding author.

Conflicts of Interest: The authors declare no conflict of interest.

References

1. Chaneliere, C.; Autran, J.L.; Devine, R.A.B.; Balland, B. Tantalum pentoxide (Ta_2O_5) thin films for advanced dielectric applications. *Mater. Sci. Eng. R* **1998**, *22*, 269–322. [CrossRef]
2. Chen, X.; Bai, R.; Huang, M. Optical properties of amorphous Ta_2O_5 thin films deposited by RF magnetron sputtering. *Opt. Mater.* **2019**, *97*, 109404. [CrossRef]
3. Porqueras, I.; Marti, J.; Bertran, E. Optical and electrical characterisation of Ta_2O_5 thin films for ionic conduction applications. *Thin Solid Films* **1999**, *343–344*, 449–452. [CrossRef]
4. Lin, H.; Ye, J.; Wang, R.; Zhu, H.; Wan, M.; Shen, K.; Mai, Y. Tailoring the microstructure and chemical composition of Ta_2O_5 solid electrolytes for application in flexible ATF-ECDs. *J. Alloys Compd.* **2022**, *918*, 165723. [CrossRef]
5. Wang, W.; Yin, F.; Niu, H.; Li, Y.; Kim, E.S.; Kim, N.Y. Tantalum pentoxide (Ta_2O_5 and Ta_2O_{5-x})-based memristor for photonic in-memory computing application. *Nano Energy* **2023**, *106*, 108072. [CrossRef]
6. Wang, R.; Pan, L.; Han, Q.; Zhu, H.; Wan, M.; Mai, Y. Reactively sputtered Ta_2O_5 solid electrolyte layers in all thin film electrochromic devices. *J. Alloys Compd.* **2021**, *865*, 158931. [CrossRef]
7. Xu, J.; Bao, X.k.; Fu, T.; Lyu, Y.; Munroe, P.; Xie, Z.-H. In vitro biocompatibility of a nanocrystalline β-Ta_2O_5 coating for orthopaedic implants. *Ceram. Int.* **2018**, *44*, 4660–4675. [CrossRef]
8. Li, J.; Dai, W.; Wu, G.; Guan, N.; Li, L. Fabrication of Ta_2O_5 films on tantalum substrate for efficient photocatalysis. *Catal. Commun.* **2015**, *65*, 24–29. [CrossRef]
9. Kaseem, M.; Fatimah, S.; Nashrah, N.; Ko, Y.G. Recent progress in surface modification of metals coated by plasma electrolytic oxidation: Principle, structure, and performance. *Prog. Mater. Sci.* **2021**, *117*, 100735. [CrossRef]
10. Simchen, F.; Sieber, M.; Kopp, A.; Lampke, T. Introduction to Plasma Electrolytic Oxidation—An Overview of the Process and Applications. *Coatings* **2020**, *10*, 628. [CrossRef]
11. Stojadinović, S.; Vasilić, R.; Perić, M. Investigation of plasma electrolytic oxidation on valve metals by means of molecular spectroscopy—A review. *RSC Adv.* **2014**, *4*, 25759–25789. [CrossRef]
12. Clyne, T.W.; Troughton, S.C. A review of recent work on discharge characteristics during plasma electrolytic oxidation of various metals. *Int. Mater. Rev.* **2018**, *64*, 127–162. [CrossRef]
13. Yerokhin, A.L.; Nie, X.; Leyland, A.; Matthews, A.; Dowey, S.J. Plasma electrolysis for surface engineering. *Surf. Coat. Technol.* **1999**, *122*, 73–93. [CrossRef]
14. Sundararajan, G.; Rama Krishna, L. Mechanisms underlying the formation of thick alumina coatings through the MAO coating technology. *Surf. Coat. Technol.* **2003**, *167*, 269–277. [CrossRef]
15. Long, B.H.; Wu, H.H.; Long, B.Y.; Wang, J.B.; Wang, N.D.; Lü, X.Y.; Jin, Z.S.; Bai, Y.Z. Characteristics of electric parameters in aluminium alloy MAO coating process. *J. Phys. D Appl. Phys.* **2005**, *38*, 3491–3496. [CrossRef]
16. Wetchakun, K.; Wetchakun, N.; Sakulsermsuk, S. An overview of solar/visible light-driven heterogeneous photocatalysis for water purification: TiO_2- and ZnO-based photocatalysts used in suspension photoreactors. *J. Ind. Eng. Chem.* **2019**, *71*, 19–49. [CrossRef]
17. Kumar, S.G.; Rao, K.S.R.K. Zinc oxide based photocatalysis: Tailoring surface-bulk structure and related interfacial charge carrier dynamics for better environmental applications. *RSC Adv.* **2015**, *5*, 3306–3351. [CrossRef]
18. Tsang, C.H.A.; Li, K.; Zeng, Y.; Zhao, W.; Zhang, T.; Zhan, Y.; Xie, R.; Leung, D.Y.C.; Huang, H. Titanium oxide based photocatalytic materials development and their role of in the air pollutants degradation: Overview and forecast. *Environ. Int.* **2019**, *125*, 200–228. [CrossRef]
19. Shandilya, P.; Sambyal, S.; Sharma, R.; Mandyal, P.; Fang, B. Properties, optimized morphologies, and advanced strategies for photocatalytic applications of WO_3 based photocatalysts. *J. Hazard. Mater.* **2022**, *428*, 128218. [CrossRef]
20. Sharma, D.; Faraz, M.; Kumar, D.; Takhar, D.; Birajdar, B.; Khare, N. Visible light activated V_2O_5/rGO nanocomposite for enhanced photodegradation of methylene blue dye and photoelectrochemical water splitting. *Inorg. Chem. Commun.* **2022**, *142*, 109657. [CrossRef]
21. Zhang, J.; Gao, Y.; Jia, X.; Wang, J.; Chen, Z.; Xu, Y. Oxygen vacancy-rich mesoporous ZrO_2 with remarkably enhanced visible-light photocatalytic performance. *Sol. Energy Mater. Sol. Cells* **2018**, *182*, 113–120. [CrossRef]
22. Ücker, C.L.; Goetzke, V.; Almeida, S.R.; Moreira, E.C.; Ferrer, M.M.; Jardim, P.L.G.; Moreira, M.L.; Raubach, C.W.; Cava, S. Photocatalytic degradation of rhodamine B using Nb_2O_5 synthesized with different niobium precursors: Factorial design of experiments. *Ceram. Int.* **2021**, *47*, 20570–20578. [CrossRef]
23. Gurylev, V. A review on the development and advancement of Ta_2O_5 as a promising photocatalyst. *Mater. Today Sustain.* **2022**, *18*, 100131. [CrossRef]
24. Chun, W.-J.; Ishikawa, A.; Fujisawa, H.; Takata, T.; Kondo, J.N.; Hara, M.; Kawai, M.; Matsumoto, Y.; Domen, K. Conduction and Valence Band Positions of Ta_2O_5, TaON, and Ta_3N_5 by UPS and Electrochemical Methods. *J. Phys. Chem. B* **2003**, *107*, 1798–1803. [CrossRef]
25. Li, Z.; He, Z.; Lai, H.; He, Y.; Zhu, Z.; Chen, Y.; Jin, T. One-step synthesis of oxygen-defects modified Ta_2O_5 nanosheets with high photocatalytic performance by chemical vapor deposition method. *Appl. Surf. Sci.* **2021**, *567*, 150776. [CrossRef]
26. Liu, W.-S.; Liao, M.-W.; Huang, S.-H.; Reyes, Y.I.A.; Tiffany Chen, H.-Y.; Perng, T.-P. Formation and characterization of gray Ta_2O_5 and its enhanced photocatalytic hydrogen generation activity. *Int. J. Hydrogen Energy* **2020**, *45*, 16560–16568. [CrossRef]

27. Tang, Y.; Huang, J.; Liu, S.; Xiang, D.; Ma, X.; Yu, X.; Li, M.; Guo, Q. Surface engineering induced superstructure Ta_2O_{5-x} mesocrystals for enhanced visible light photocatalytic antibiotic degradation. *J. Colloid Interface Sci.* **2021**, *596*, 468–478. [CrossRef]
28. Fu, H.; Chen, F.; Wang, Y.; Yang, X.; Xiong, S.; An, X. High adsorption and photocatalytic degradation abilities of amorphous Ta_2O_5 nanospheres under simulated solar light irradiation. *J. Photochem. Photobiol. A* **2022**, *433*, 114193. [CrossRef]
29. Stojadinović, S.; Radić, N.; Tadić, N.; Vasilić, R.; Stefanov, P.; Grbić, B. Influence of iron doping on photocatalytic activity of TiO_2 coatings formed on titanium by plasma electrolytic oxidation. *J. Mater. Sci.-Mater. Electron.* **2018**, *29*, 9427–9434. [CrossRef]
30. Stojadinović, S.; Vasilić, R.; Radić, N.; Tadić, N.; Stefanov, P.; Grbić, B. The formation of tungsten doped Al_2O_3/ZnO coatings on aluminum by plasma electrolytic oxidation and their application in photocatalysis. *Appl. Surf. Sci.* **2016**, *377*, 37–43. [CrossRef]
31. Stojadinović, S.; Radić, N.; Vasilić, R. Photoluminescent and Photocatalytic Properties of Eu^{3+}-Doped MgAl Oxide Coatings Formed by Plasma Electrolytic Oxidation of AZ31 Magnesium Alloy. *Coatings* **2022**, *12*, 1830. [CrossRef]
32. Sowa, M.; Kazek-Kęsik, A.; Socha, R.P.; Dercz, G.; Michalska, J.; Simka, W. Modification of tantalum surface via plasma electrolytic oxidation in silicate solutions. *Electrochim. Acta* **2013**, *114*, 627–636. [CrossRef]
33. Sowa, M.; Woszczak, M.; Kazek-Kęsik, A.; Dercz, G.; Korotin, D.M.; Zhidkov, I.S.; Kurmaev, E.Z.; Cholakh, S.O.; Basiaga, M.; Simka, W. Influence of process parameters on plasma electrolytic surface treatment of tantalum for biomedical applications. *Appl. Surf. Sci.* **2017**, *407*, 52–63. [CrossRef]
34. Antonio, R.F.; Rangel, E.C.; Mas, B.A.; Duek, E.A.R.; Cruz, N.C. Growth of hydroxyapatite coatings on tantalum by plasma electrolytic oxidation in a single step. *Surf. Coat. Technol.* **2019**, *357*, 698–705. [CrossRef]
35. Cheng, Y.; Zhang, Q.; Zhu, Z.; Tu, W.; Cheng, Y.; Skeldon, P. Potential and morphological transitions during bipolar plasma electrolytic oxidation of tantalum in silicate electrolyte. *Ceram. Int.* **2020**, *46*, 13385–13396. [CrossRef]
36. Petković, M.; Stojadinović, S.; Vasilić, R.; Zeković, L. Characterization of oxide coatings formed on tantalum by plasma electrolytic oxidation in 12-tungstosilicic acid. *Appl. Surf. Sci.* **2011**, *257*, 10590–10594. [CrossRef]
37. Lv, J.; Cheng, Y. Amorphous coatings on tantalum formed by plasma electrolytic oxidation in aluminate electrolyte and high temperature crystallization treatment. *Surf. Coat. Technol.* **2022**, *434*, 128171. [CrossRef]
38. Stojadinović, S.; Radić, N.; Vasilić, R. ZnO Particles modified MgAl Coatings with improved photocatalytic activity formed by plasma electrolytic oxidation of AZ31 magnesium alloy in aluminate electrolyte. *Catalysts* **2022**, *12*, 1503. [CrossRef]
39. Stojadinović, S.; Tadić, N.; Vasilić, R. Luminescence of oxide films during the electrolytic oxidation of tantalum. *Electrochim. Acta* **2015**, *152*, 323–329. [CrossRef]
40. Albella, J.M.; Montero, I.; Martinez-Duart, J.M. A theory of avalanche breakdown during anodic oxidation. *Electrochim. Acta* **1987**, *32*, 255–258. [CrossRef]
41. Ikonopisov, S. Theory of electrical breakdown during formation of barrier anodic films. *Electrochim. Acta* **1977**, *22*, 1077–1082. [CrossRef]
42. Klapkiv, M.D.; Nykyforchyn, H.M.; Posuvailo, V.M. Spectral analysis of an electrolytic plasma in the process of synthesis of aluminum oxide. *Mater. Sci.* **1995**, *30*, 333–343. [CrossRef]
43. Kasalica, B.; Stojadinović, S.; Belča, I.; Sarvan, M.; Zeković, L.; Radić-Perić, J. The anomalous sodium doublet D_2/D_1 spectral line intensity ratio—A manifestation of CCD's presaturation effect. *J. Anal. At. Spectrom.* **2013**, *28*, 92–97. [CrossRef]
44. Stojadinović, S.; Jovović, J.; Petković, M.; Vasilić, R.; Konjević, N. Spectroscopic and real-time imaging investigation of tantalum plasma electrolytic oxidation (PEO). *Surf. Coat. Technol.* **2011**, *205*, 5406–5413. [CrossRef]
45. Ivković, M.; Jovićević, S.; Konjević, N. Low electron density diagnostics: Development of optical emission spectroscopic techniques and some applications to microwave induced plasmas. *Spectrochim. Acta Part B* **2004**, *59*, 591–605. [CrossRef]
46. Hussein, R.O.; Nie, X.; Northwood, D.O.; Yerokhin, A.; Matthews, A. Spectroscopic study of electrolytic plasma and discharging behaviour during the plasma electrolytic oxidation (PEO) process. *J. Phys. D Appl. Phys.* **2010**, *43*, 105203. [CrossRef]
47. Lodi, T.A.; Galleani, G.; Merízio, L.G.; Jacobsohn, L.G.; Mastelaro, V.R.; de Camargo, A.S.S. Tungsten gallium-phosphate glasses as promising intrinsic scintillators. *J. Non-Cryst. Solids* **2023**, *603*, 122097. [CrossRef]
48. Jiménez-Morales, I.; Santamaría-González, J.; Maireles-Torres, P.; Jiménez-López, A. Mesoporous tantalum phosphate as acidic catalyst for the methanolysis of sunflower oil. *Appl. Catal. B* **2012**, *123–124*, 316–323. [CrossRef]
49. Stojadinović, S.; Radić, N.; Grbić, B.; Maletić, S.; Stefanov, P.; Pačevski, A.; Vasilić, R. Structural, photoluminescent and photocatalytic properties of TiO_2:Eu^{3+} coatings formed by plasma electrolytic oxidation. *Appl. Surf. Sci.* **2016**, *370*, 218–228. [CrossRef]
50. Stojadinović, S.; Tadić, N.; Radić, N.; Grbić, B.; Vasilić, R. MgO/ZnO coatings formed on magnesium alloy AZ31 by plasma electrolytic oxidation: Structural, photoluminescence and photocatalytic investigation. *Surf. Coat. Technol.* **2017**, *310*, 98–105. [CrossRef]
51. Stojadinović, S.; Vasilić, R.; Radić, N.; Grbić, B. Zirconia films formed by plasma electrolytic oxidation: Photoluminescent and photocatalytic properties. *Opt. Mater.* **2015**, *40*, 20–25. [CrossRef]
52. Stojadinović, S.; Tadić, N.; Radić, N.; Stefanov, P.; Grbić, B.; Vasilić, R. Anodic luminescence, structural, photoluminescent, and photocatalytic properties of anodic oxide films grown on niobium in phosphoric acid. *Appl. Surf. Sci.* **2015**, *355*, 912–920. [CrossRef]
53. Ai, M.; Zhang, J.; Wu, Y.; Pan, L.; Shi, C.; Zou, J. Role of Vacancies in Photocatalysis: A Review of Recent Progress. *Chem. Asian J.* **2020**, *15*, 3599–3619. [CrossRef] [PubMed]
54. Bai, S.; Zhang, N.; Gao, C.; Xiong, Y. Defect engineering in photocatalytic materials. *Nano Energy* **2018**, *53*, 296–336. [CrossRef]

55. Liqiang, J.; Yichun, Q.; Baiqi, W.; Shudan, L.; Baojiang, J.; Libin, Y.; Wei, F.; Honggang, F.; Jiazhong, S. Review of photoluminescence performance of nano-sized semiconductor materials and its relationships with photocatalytic activity. *Sol. Energy Mater. Sol. Cells* **2006**, *90*, 1773–1787. [CrossRef]
56. Nakajima, H.; Mori, T. Photoluminescence excitation bands corresponding to defect states due to oxygen vacancies in yttria-stabilized zirconia. *J. Alloys Compd.* **2006**, *408–412*, 728–731. [CrossRef]
57. Liqiang, J.; Xiaojun, S.; Baifu, X.; Baiqi, W.; Weimin, C.; Honggan, F. The preparation and characterization of La doped TiO_2 nanoparticles and their photocatalytic activity. *J. Solid State Chem.* **2004**, *177*, 3375–3382. [CrossRef]